

Comparing OMI-TOMS and OMI-DOAS total ozone column data

M. Kroon,¹ J. P. Veefkind,¹ M. Sneep,¹ R. D. McPeters,² P. K. Bhartia,² and P. F. Levelt¹

Received 13 April 2007; revised 18 September 2007; accepted 7 December 2007; published 23 May 2008.

[1] The Ozone Monitoring Instrument (OMI) project team uses two total ozone retrieval algorithms in order to maintain the long-term record established with Total Ozone Mapping Spectrometer (TOMS) data as well as to improve the ozone column estimate using the hyperspectral capability of OMI. The purpose of this study is to assess where the algorithms produce comparable results and where the differences are significant. Starting with the same set of Earth reflectance data, the total ozone data used in this study have been derived using OMI-TOMS and OMI-Differential Optical Absorption Spectroscopy (DOAS) algorithms. OMI-TOMS is based on the TOMS version 8 algorithm that has been used to process TOMS data taken since November 1978. The OMI-DOAS retrieval algorithm was developed specifically for OMI. It takes advantage of the hyperspectral feature of the OMI instrument to reduce errors due to aerosols, clouds, surface, and sulfur dioxide from volcanic eruptions. The OMI-DOAS algorithm also has improved correction for cloud height. The mean differences in the ozone column derived from the two algorithms vary from 0 to 9 DU (0–3%), and their correlation coefficients vary between 0.89 and 0.99 with latitude and season. The largest differences occur in the polar regions and over clouds. Some of the differences are due to stray light, dark current, and other instrumental errors that have been corrected in the new version of the OMI radiance/irradiance data set (collection 3). Other differences are algorithmic. OMI-DOAS algorithmic errors identified through this analysis are also being corrected in collection 3 reprocessing. However, for consistency with the long-term TOMS record, OMI-TOMS collection 3 data will still be based on the TOMS V8 algorithm. Preliminary analysis shows much better agreement in the two total ozone data sets after reprocessing. Reprocessed collection 3 data from both algorithms will be available before the end of 2007. Continuing the TOMS total ozone column data record that dates back to November 1978 is the primary OMI mission goal that is achievable with either OMI total ozone column data product.

Citation: Kroon, M., J. P. Veefkind, M. Sneep, R. D. McPeters, P. K. Bhartia, and P. F. Levelt (2008), Comparing OMI-TOMS and OMI-DOAS total ozone column data, *J. Geophys. Res.*, 113, D16S28, doi:10.1029/2007JD008798.

1. Introduction

[2] The Dutch-Finnish Ozone Monitoring Instrument (OMI) [Levelt *et al.*, 2006a, 2006b] aboard the NASA Earth Observing System (EOS) Aura satellite [Schoeberl *et al.*, 2006] is a compact nadir viewing, wide swath, ultraviolet-visible (270–500 nm) hyperspectral imaging spectrometer that provides daily global coverage with high spatial and spectral resolution. The Aura orbit is Sun-synchronous at 705 km altitude with a 98° inclination and ascending node equator-crossing time roughly at 1345 local time (LT). OMI measures backscattered solar radiance in the dayside portion of each orbit and solar irradiance near the Northern Hemisphere terminator once per day. The OMI data products are derived from the ratio of Earth radiance and solar irradiance. In this paper we compare the output of the

OMI-Differential Optical Absorption Spectroscopy (DOAS) [Bhartia and Wellemeyer, 2002; Veefkind *et al.*, 2006] and OMI-Total Ozone Mapping Spectrometer (TOMS) [Bhartia and Wellemeyer, 2002; Balis *et al.*, 2007; McPeters *et al.*, 2008] total ozone column retrieval algorithms. (Please read the README files of these data product carefully prior to use. OMI README files are available at <http://disc.gsfc.nasa.gov/Aura/OMI/>.) The OMI-TOMS algorithm is based on the TOMS V8 algorithm that has been used to process data from a series of four TOMS instruments flown since November 1978. This algorithm uses measurements at 4 discrete 1 nm wide wavelength bands centered at 313, 318, 331 and 360 nm. The OMI-DOAS algorithm [Veefkind *et al.*, 2006] takes advantage of the hyperspectral feature of OMI. It is based on the principle of Differential Optical Absorption Spectroscopy (DOAS) [Perner and Platt, 1979]. The algorithm uses ~25 OMI measurements in the wavelength range 331.1 nm to 336.6 nm, as described by Veefkind *et al.* [2006]. The key difference between the two algorithms is that the DOAS algorithm removes the effects of aerosols, clouds, volcanic

¹Royal Netherlands Meteorological Institute, De Bilt, Netherlands.

²NASA Goddard Space Flight Center, Greenbelt, Maryland, USA.

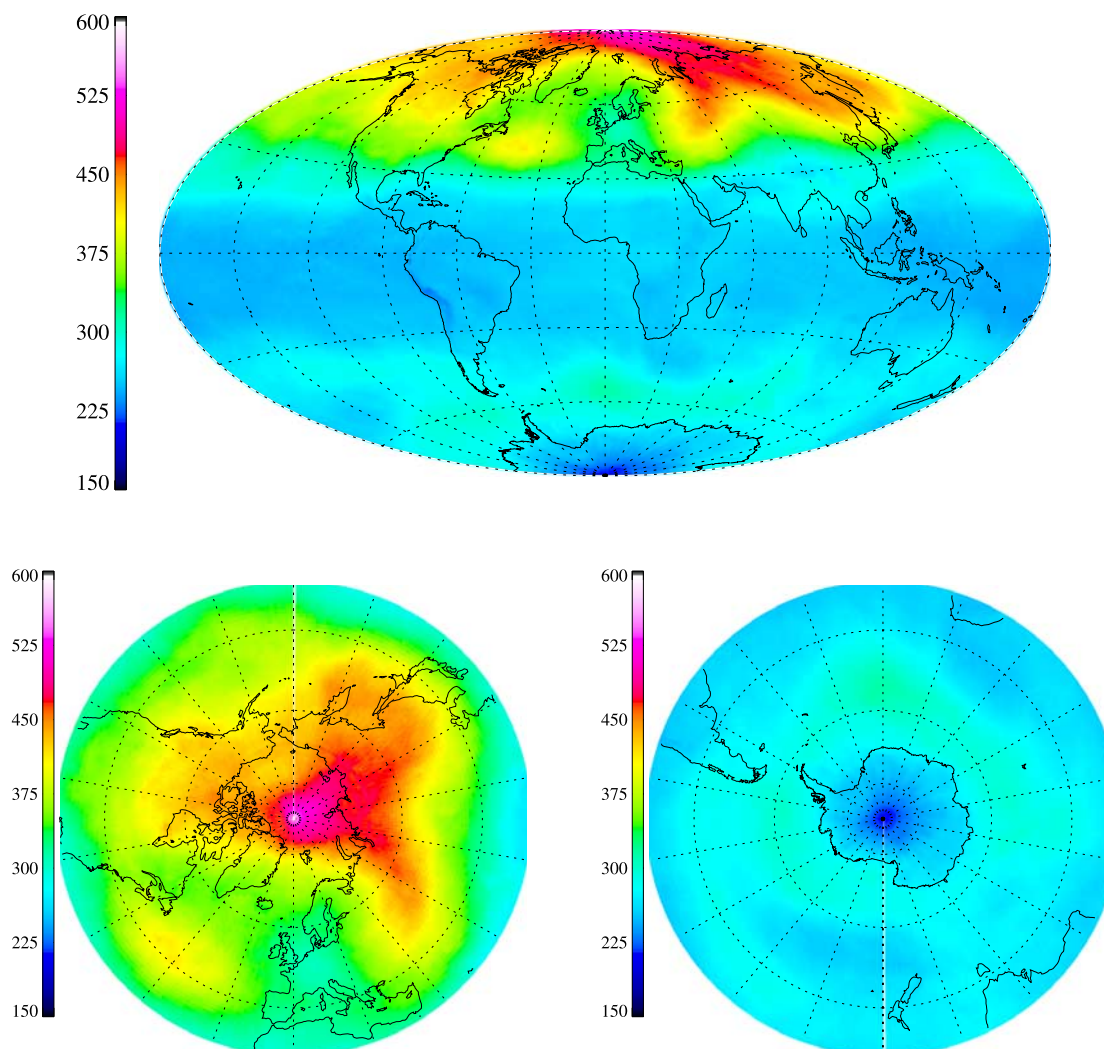


Figure 1. Global distribution of Ozone Monitoring Instrument–Total Ozone Mapping Spectrometer (OMI-TOMS) total column ozone expressed in Dobson units regridded to a 180×360 grid ($1.0^\circ \times 1.0^\circ$ resolution). The data are from the time period 21–27 March 2005, and are presented in the Mollweide projection and polar top views. Note the large dynamical range of total ozone columns over the globe.

sulfur dioxide, and surface effects by spectral fitting while the TOMS algorithm applies an empirical correction to remove these effects. In addition, the TOMS algorithm uses a cloud height climatology that was derived using infrared satellite data, while the DOAS algorithm uses cloud information derived from OMI measurements in the 470 nm $\text{O}_2\text{-O}_2$ absorption band. The two algorithms also respond to instrumental errors very differently. The purpose of this study is to assess the quality of the OMI-DOAS and OMI-TOMS total ozone column data product by their similarities and their differences, and to associate these differences with particular characteristics of the retrievals. We first compare global images of the total ozone columns from the two algorithms to check whether they render the same patterns and structures. We then look more quantitatively at the correlation and proportionality between the two data sets. We report differences between OMI-TOMS and OMI-DOAS total ozone columns in global images, as a function of various parameters describing the measurements

geometry, and as a function of atmospheric quantities measured over the same ground pixel.

2. Data and Analysis

[3] OMI level 2 data comes in the form of orbit files that contain trace gas abundances as retrieved on the day side of the Aura orbit from the level 1B reflectance spectra. OMI level 2 data products used in this study are OMI-DOAS total ozone column, labeled OMDOAO3; OMI-TOMS total ozone column, labeled OMT03; and OMI total sulfur dioxide column, labeled OMSO2. The data were obtained from the OMI Science Investigator-led Processing System (OSIPS) of Earth Observing System Data and Information System Core System (ECS) collection 2. The time period covered is from September 2004 to June 2007. From the start of the OMI data record, the results of validation exercises have been used to identify OMI-DOAS algorithm shortcomings and to provide insights into where retrieval algorithm improvements were needed. The implementation

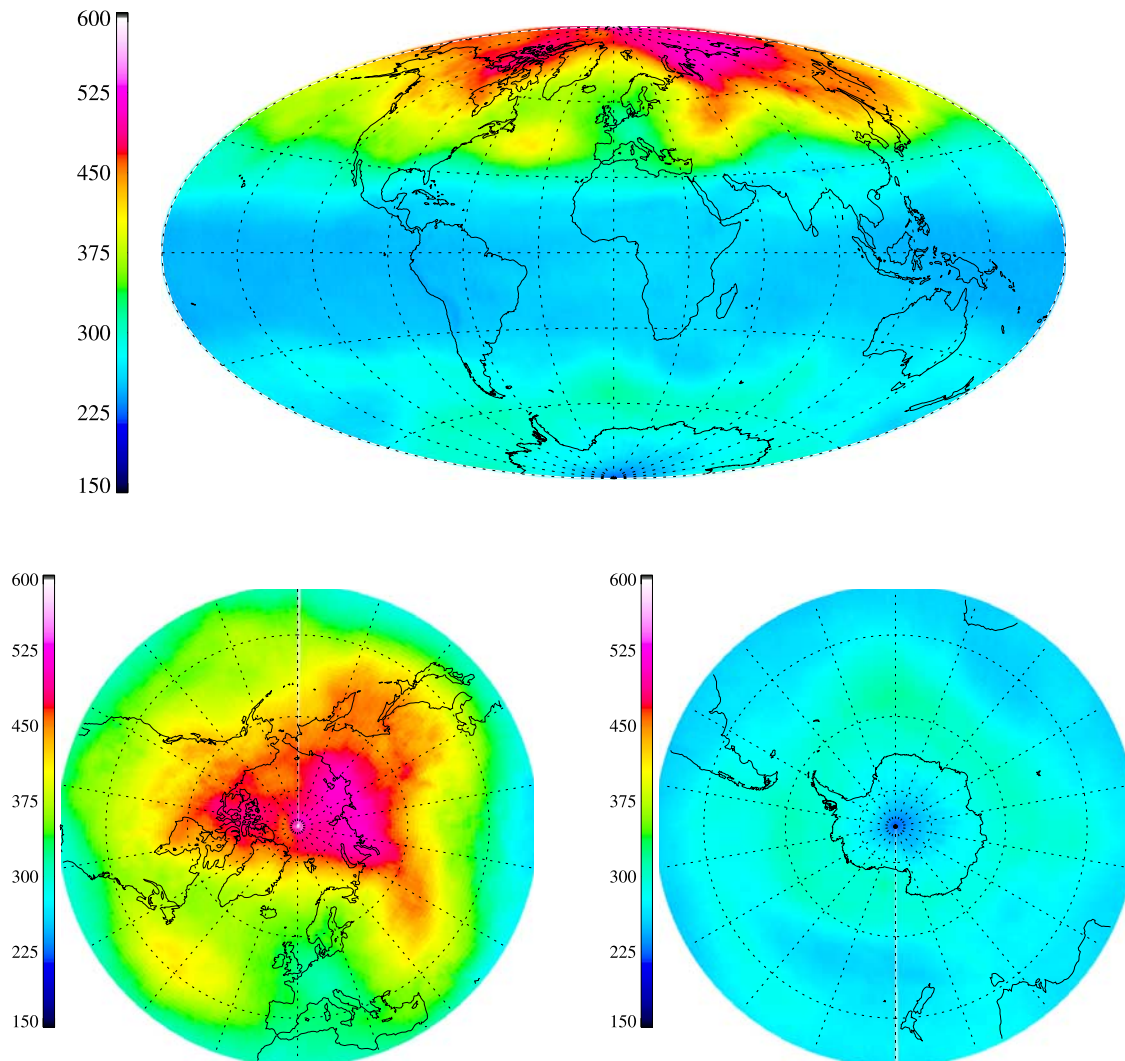


Figure 2. Global distribution of OMI–Differential Optical Absorption Spectroscopy (DOAS) total column ozone expressed in Dobson units regridded to a 180×360 grid ($1.0^\circ \times 1.0^\circ$ resolution). The data are from the time period 21–27 March 2005, and are presented in the Mollweide projection and polar top views. Note the structures similar to those presented in Figure 1.

of these improvements has resulted in the release of a number of versions of the software. Data collected between September 2004 and October 2005 was processed with software version v0.9.4. From October 2005 onward v1.0.1 has been operational. The absolute differences between these versions are minor, much smaller than the retrieval accuracy. Therefore we consider the OMI-DOAS data record as continuous. At the time of writing, the further optimized OMI-DOAS algorithm is ready for reprocessing the OMI data record into collection 3.

[4] Data analysis is performed with the CAMA toolbox written by Maarten Snee of KNMI (CAMA, 2006: For more information, please visit our Web site, <http://www.knmi.nl/omi/research/validation/cama/>, where the CAMA software can be downloaded and documentation can be obtained. CAMA runs under IDL.). CAMA stands for “Correleer Alles Met Alles,” literally meaning “correlate everything with everything.” This toolbox can be instructed to read an OMI level 2 data set described

by a range of orbit numbers, and per orbit file read a set of data fields. Data is filtered synchronously on the basis of the values of quality flags and limits set. Synchronous filtering of the data fields in OMI orbit data means that when the value of a certain data field does not pass the filter conditions imposed, that pixel position is filled with a Not-A-Number value in all data fields to be ignored by the subsequent calculations. The CAMA toolbox allows not only exploration of a single OMI data product, for example OMI-DOAS total ozone column and its cloud fraction, and the relation between these data fields, but also the exploration of interdependencies of two or more OMI data products, for example OMI-DOAS and OMI-TOMS, and the correlation of their differences with respect to, e.g., cloud fraction, cloud pressure, snow/ice coverage and other OMI trace gases. The toolbox performs a statistical analysis of all read quantities and preinstructed derivatives per ground pixel, yielding frequency distributions and along-track

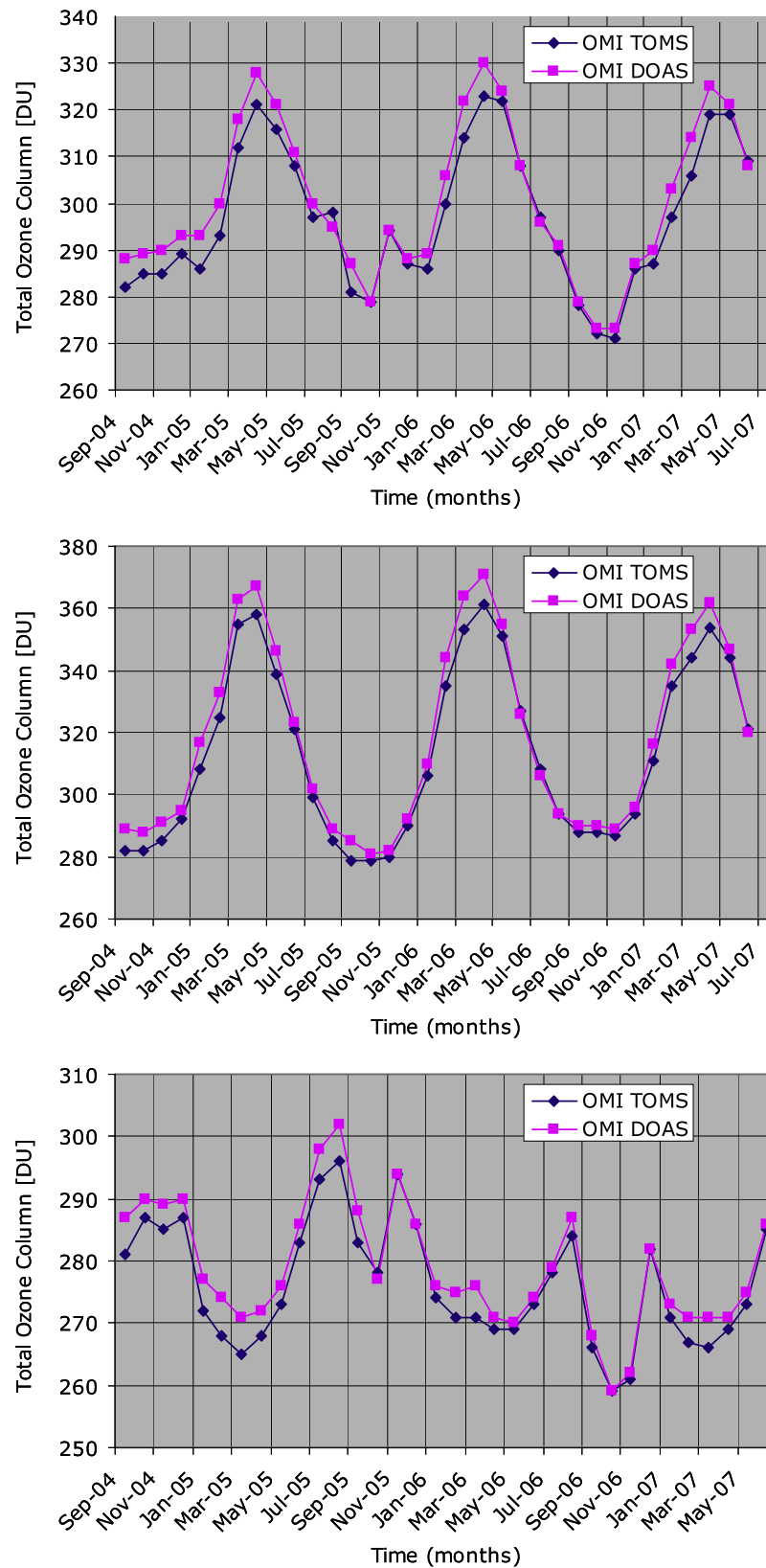


Figure 3. Graphical representation of the OMI total ozone column data products versus time (from top to bottom) as averaged over the whole globe, the Northern Hemisphere, and the Southern Hemisphere. Note the 2006 record ozone hole significantly lowering globally averaged ozone. Please note the different dynamic range for all three plots.

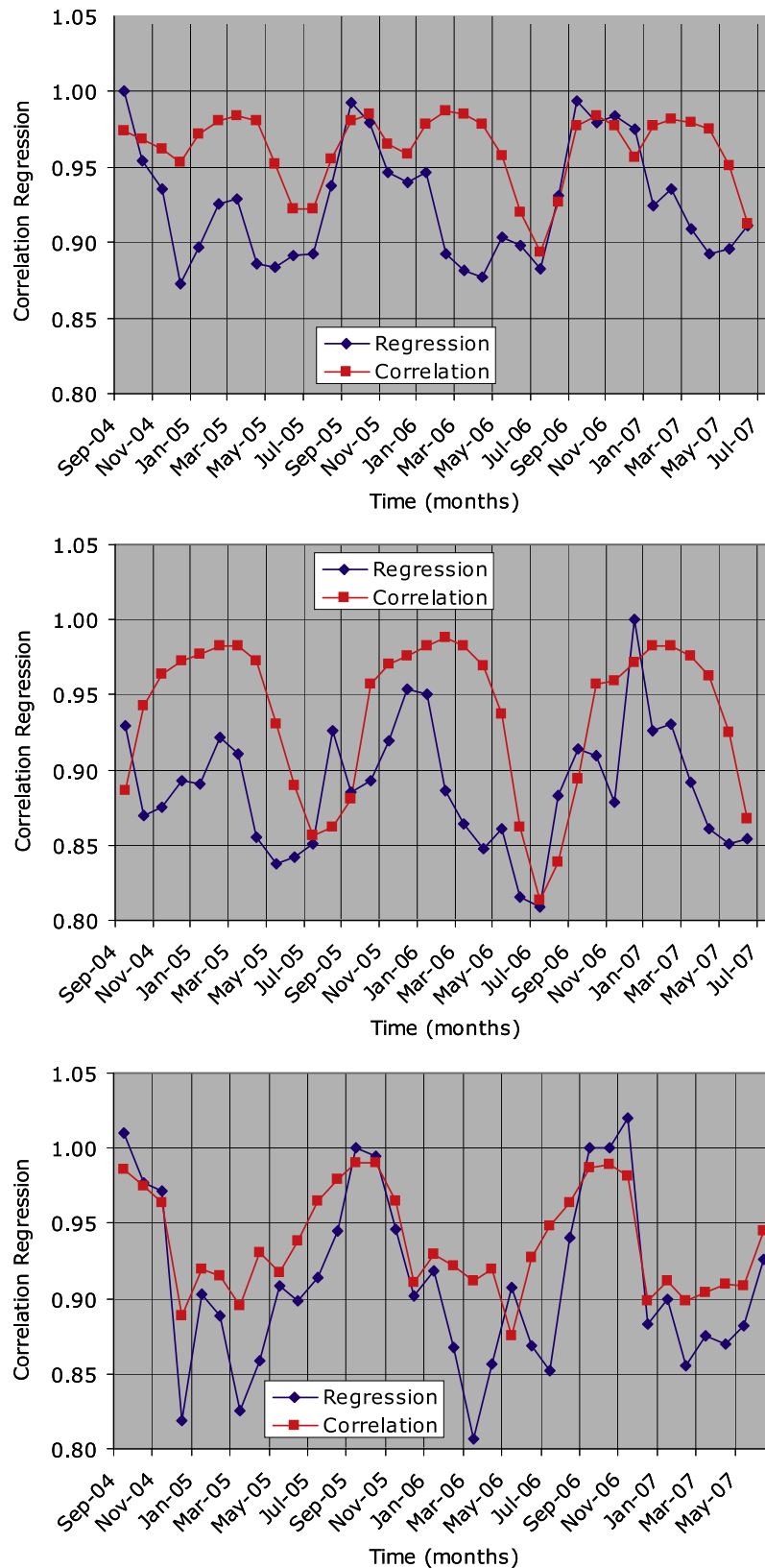


Figure 4. Graphical representation of the correlation and regression coefficient of OMI-TOMS and OMI-DOAS total ozone column versus time for (from top to bottom), the whole globe, the Northern and Southern hemispheres. Note the high degree of correlation and proportionality between both OMI total ozone data products over the entire data record.

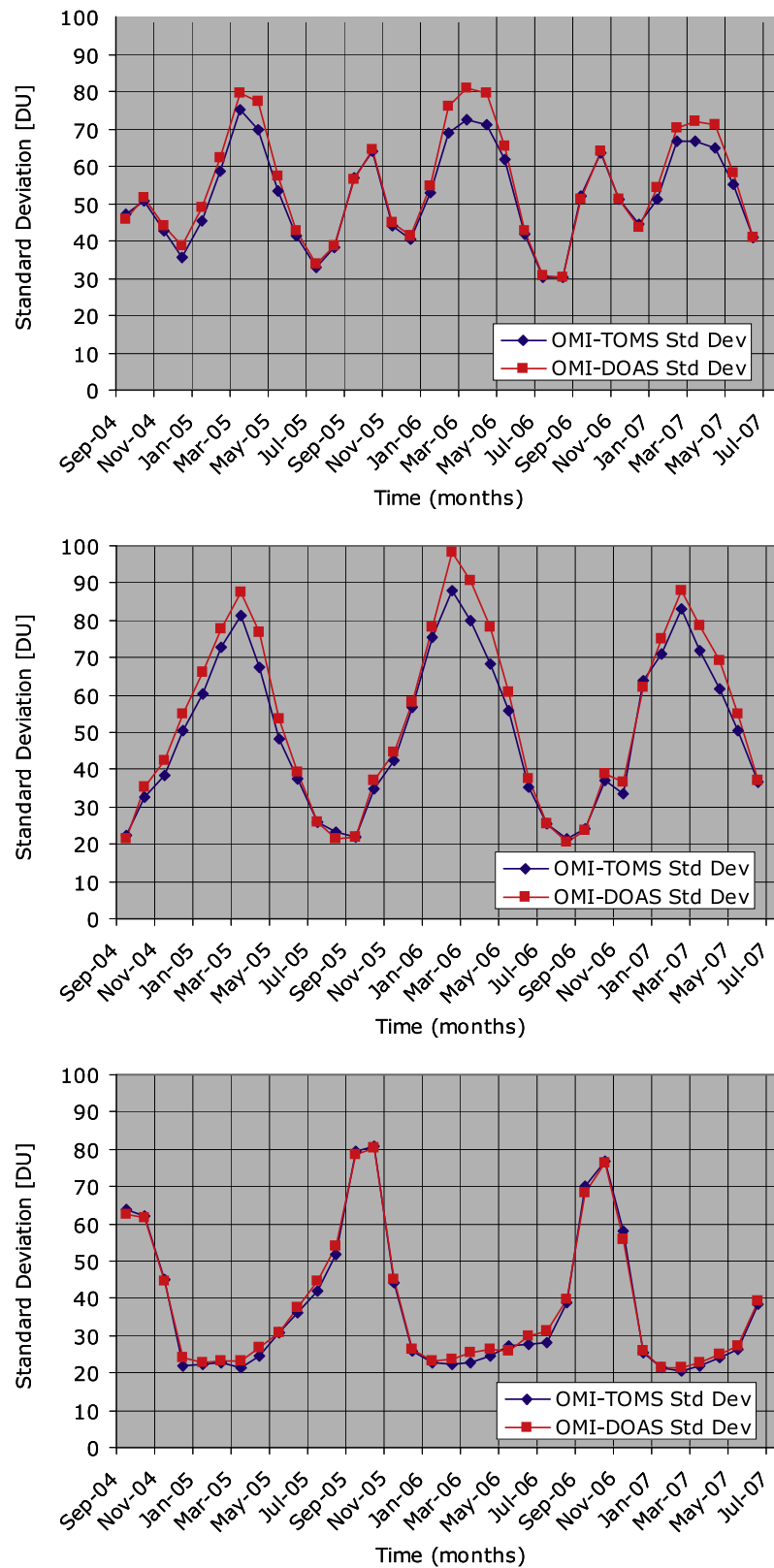


Figure 5. Graphical representation of the standard deviation of the OMI-TOMS and OMI-DOAS total ozone column versus time for (from top to bottom), the whole globe, the Northern and Southern hemispheres.

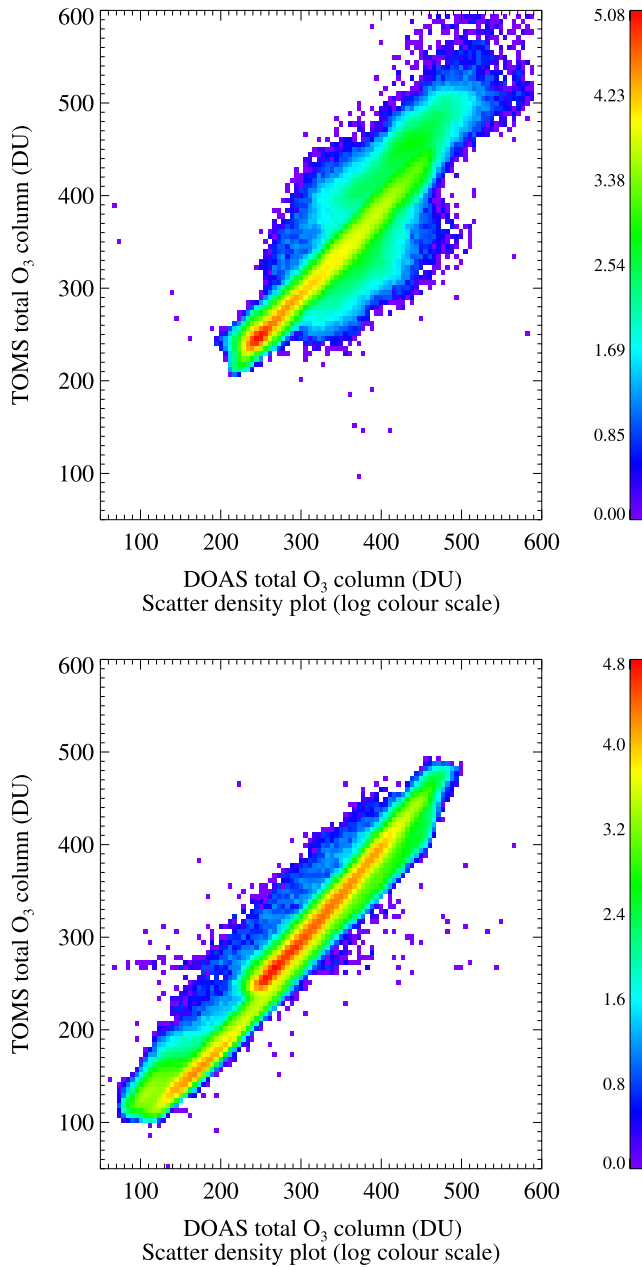


Figure 6. Logarithmic (base 10) scatter density plots of OMI-TOMS versus OMI-DOAS total ozone columns in the Northern Hemisphere for the time period 14 to 20 December 2004 (top) and in the Southern Hemisphere for the time period 14 to 20 September 2005 (bottom). Note the bimodal distribution in the Southern Hemisphere data during the occurrence of the ozone hole.

averages of the individual quantities. The toolbox also calculates scatter density plots, and tables describing statistical averages and standard deviations, correlation and covariance coefficients, skewness and kurtosis coefficients, and regression coefficients for all combinations of parameters. These analyses have been performed for the whole globe and for the Northern and Southern hemispheres separately to study the different behavior of OMI data products in both hemispheres. To study the effect of volcanic emissions of sulfur dioxide on OMI

total ozone columns, regional comparisons have been made incorporating OMI data zoomed into a region of interest near volcanic eruptions. Such an approach reveals the strong local effects of these emissions which are otherwise obscured by global statistics. In addition, the CAMA toolbox calculates global distributions of all read quantities by means of regridding to a latitude-longitude grid with a resolution predefined by the user yielding, e.g., global images of OMI-DOAS and OMI-TOMS total ozone columns and their differences. The regridding is performed by averaging all OMI data points for which the pixel center coordinates fall within that particular grid cell. Because regridded data is used here for visualization purposes only, no advanced weighing is applied. The global images obtained reveal the global structures of the read data sets and those features that depend on geography.

3. Global Distributions of Total Ozone Column

[5] Figures 1 and 2 show the global distribution of OMI-TOMS and OMI-DOAS total ozone column, respec-

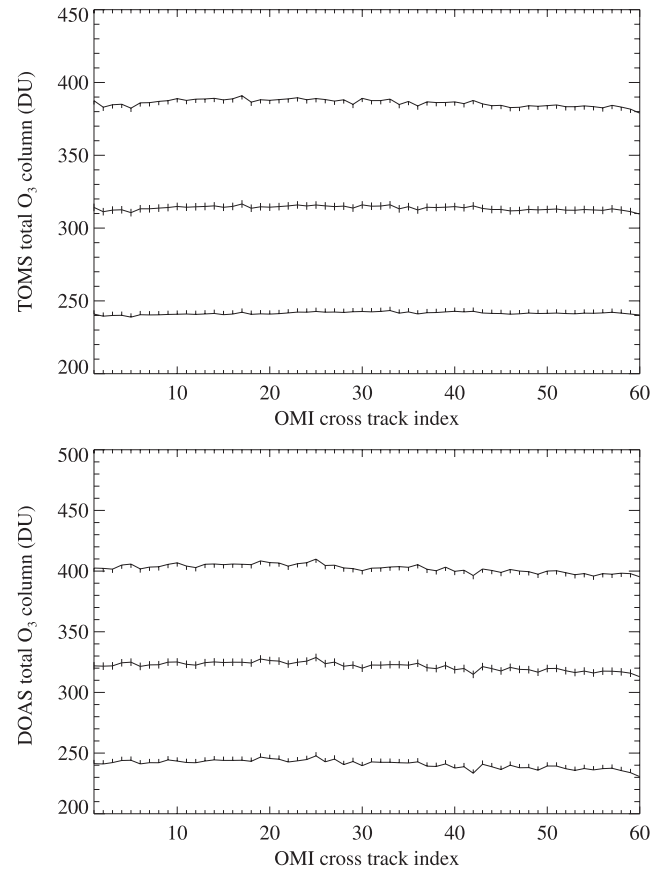


Figure 7. Global along-track averages of total ozone column for OMI-TOMS (top) and OMI-DOAS (bottom) for the time period 14 to 27 March 2006 of OMI cross track positions. In these graphs the middle line denotes the total ozone column averaged over the time period mentioned for each OMI track position, ranging from 1 to 60, individually. The lines above and below the mean denote the mean plus or minus one standard deviation for each ground pixel individually.

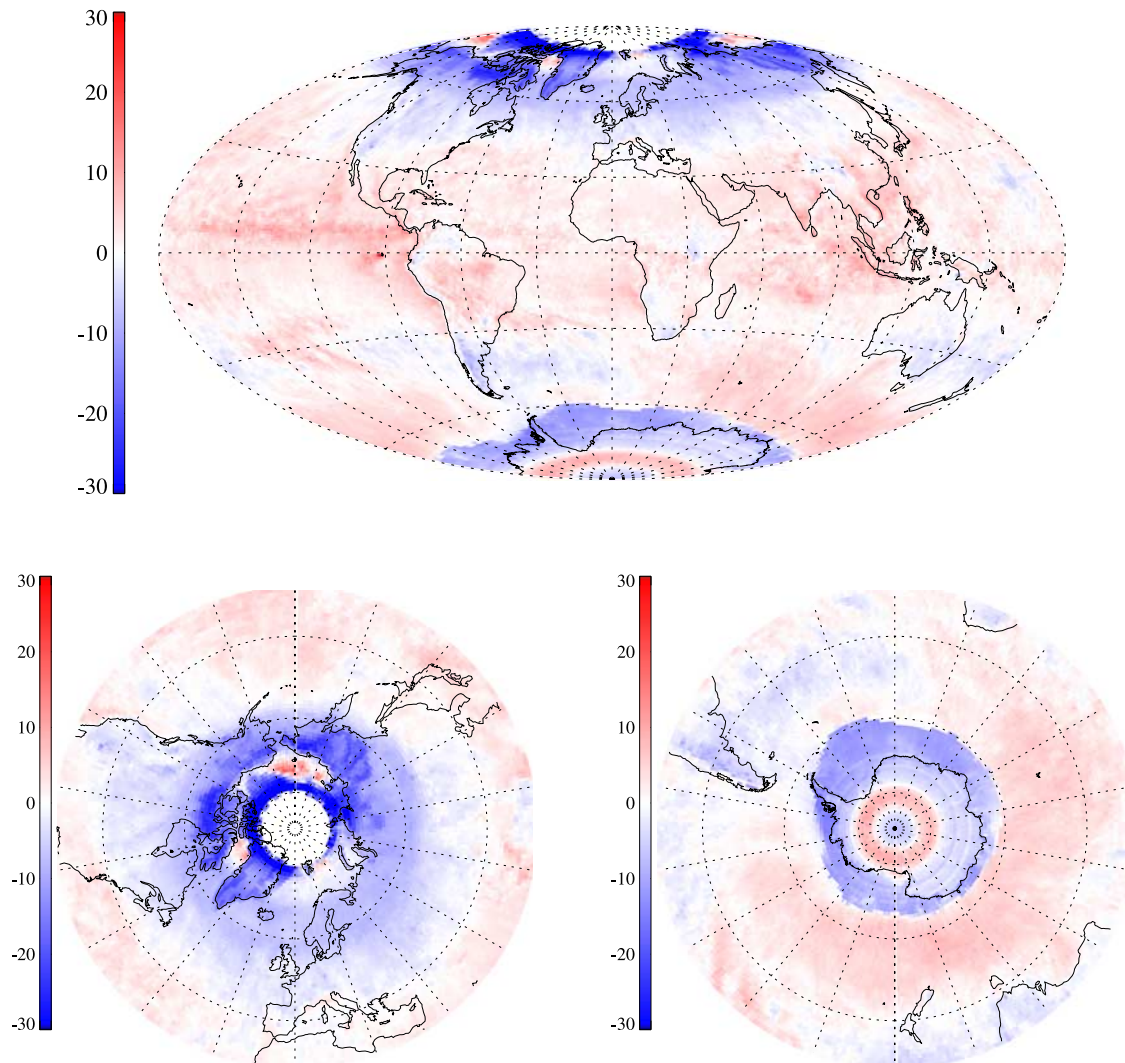


Figure 8. Global distribution of OMI-TOMS and OMI-DOAS total column ozone difference expressed in Dobson units regridded to a 180×360 grid ($1.0^\circ \times 1.0^\circ$ resolution). The data are from the time period 14 to 27 October 2005, and are presented in the Mollweide projection and polar top views. Note the visibility of sea ice structures around Antarctica, the dark blue structures at the high latitudes in the Northern Hemisphere and a volcanic eruption at the Galapagos Islands in the east Pacific Ocean.

tively. Each image is obtained by regridding OMI data for the time period 21 to 27 March 2005, consisting of 102 orbits, to a latitude-longitude grid of $1.0^\circ \times 1.0^\circ$ resolution (180×360). A comparison of Figures 1 and 2 reveals very similar structures in OMI-TOMS and OMI-DOAS total ozone columns. There are no obvious geographical dependencies observed. Results for other time periods look very similar.

[6] Figures 3, 4, and 5 provide a statistical comparison of OMI-TOMS and OMI-DOAS total column ozone data during the time period September 2004 to June 2007. Results are reported separately for the whole globe and for the Northern (NH) and Southern (SH) hemispheres for days 14 to 27 of each month. These time intervals are centered on the equinox and solstice dates. Figure 3 shows that globally averaged OMI-TOMS and OMI-DOAS total ozone columns are in close agreement over the OMI data record and show a similar annual cycle of 25–30 DU amplitude. On the global scale, OMI-TOMS reports

0–8 DU less total ozone column than OMI-DOAS, depending on the season. Differences are largest during late spring (May) and early summer (June). The record breaking 2006 ozone hole significantly lowered globally averaged ozone in the SH spring of 2006. Figure 3 shows that both OMI-TOMS and OMI-DOAS hemispheric averages show a similar annual cycle of ~ 40 DU (NH) and ~ 20 DU (SH) amplitude. More obviously, there is a 6 month phase shift between the two hemispheres, but the timing of the minima/maxima in the SH is erratic and is strongly affected (presumably) by interannually varying ozone hole effects.

[7] Figure 4 shows that both total ozone data products correlate well over the OMI data record; the correlation coefficients range from 0.89 to 0.99, depending on season. The regression coefficients range from 0.87 to unity, which shows that the two data sets vary linearly against each other. The near unity regression and correlation in the Southern Hemisphere during the ozone hole season indicates good

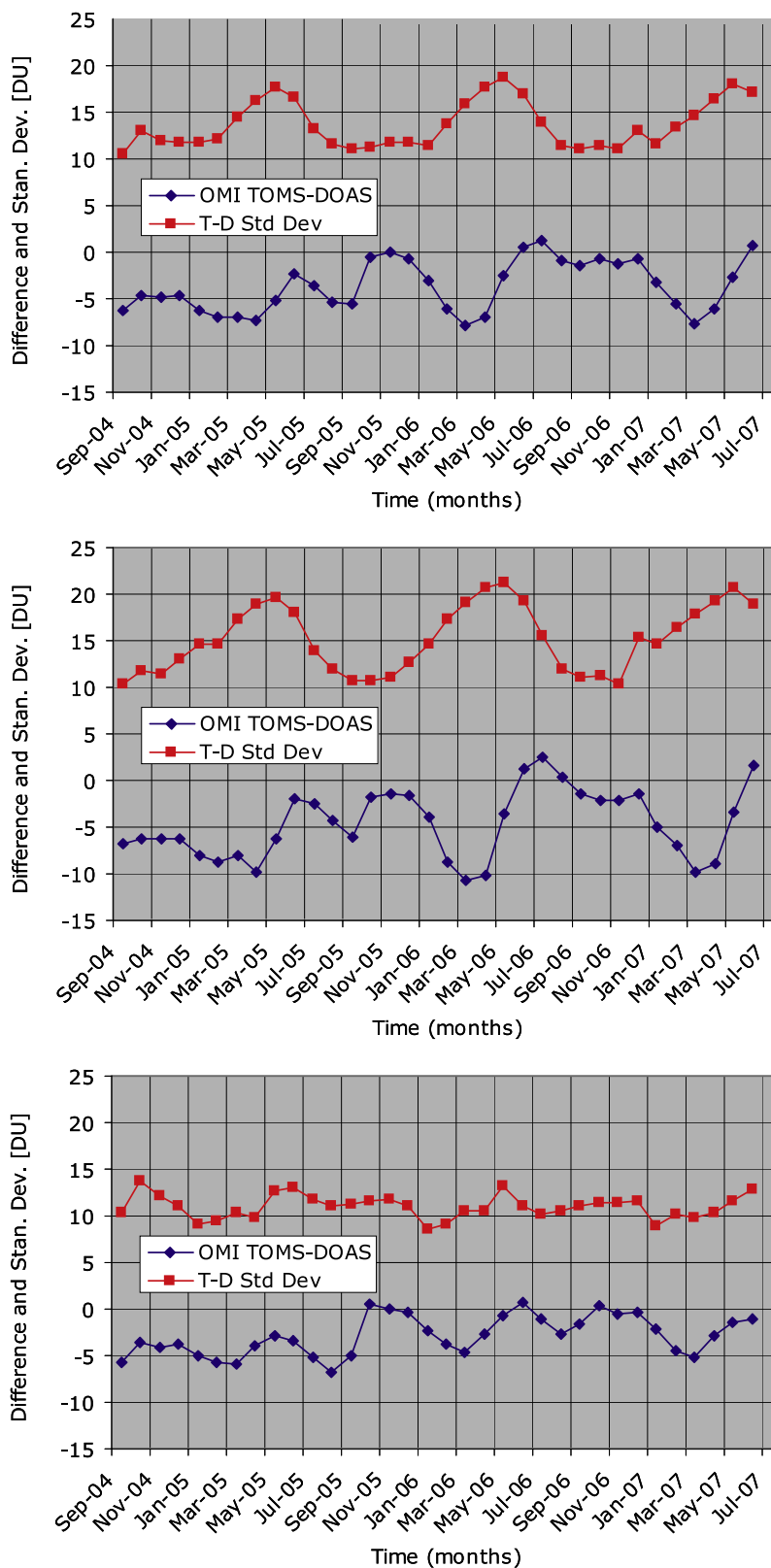


Figure 9. Graphical representation of the total ozone column difference (OMI-TOMS minus OMI DOAS) and its standard deviation versus time for (from top to bottom), the whole globe, the Northern and Southern hemispheres.

agreement between the two data sets over a wide range of total column values where minimum columns reach below 100 DU. In the Northern Hemisphere their different behavior, particularly over snow and ice, reduced the regression coefficient.

[8] The regression coefficient is the correlation coefficient multiplied by the ratio of the standard deviations of the two total ozone columns. This statement follows directly from using the matrix elements of the covariance matrix for calculating these quantities. Given the high correlations coefficients, additional information supplied by the regression coefficient is the ratio of these standard deviations which are physical measures of the natural variability of the total ozone column. On average Figure 4 indicates that OMI-TOMS ozone is varying to some extent less than OMI-DOAS ozone. This observation is exemplified by Figure 5 which shows that the standard deviation of the OMI-TOMS and OMI-DOAS total ozone column for the OMI data record are in close agreement even though both fluctuate strongly depending on season. The natural variability on both hemispheres runs approximately half a year out of phase, and is dominated on the Southern Hemisphere by the variability of the ozone hole.

[9] In Figure 6 we show the scatter density plots of OMI-TOMS versus OMI-DOAS total ozone column on a logarithmic (base 10) color scale for two different time periods for the Northern and Southern hemispheres. Scatter densities represent the statistical occurrence of pairs of values from both axis. The strong correlation between OMI-TOMS and OMI-DOAS total ozone columns in both hemispheres is evident from the graphs. In the Southern Hemisphere the correlation is as pronounced as in the Northern Hemisphere, although covering a smaller dynamic range during most of the year. During the Southern Hemisphere ozone hole season, from September to December, the statistics for the Southern Hemisphere appear to become bimodal with the collection of data points in the lower left corner associated with the ozone hole. The observation of this bimodal distribution highlights the extreme conditions of the ozone hole. There are almost no total ozone column observations between 200 and 230 DU indicating that entering the vortex represents a dramatic transition from normal ozone conditions to extremely low ozone conditions, even when resolved by OMI. The signature of the bimodal distribution is strongest when the ozone hole is deepest and weakens as the meteorological polar vortex weakens with the arrival of local spring.

[10] The OMI ground swath of 2600 km wide is divided into 60 ground pixels, where positions 29, 30 denote the exact subsatellite positions [Levelt, 2002]. All OMI data products are retrieved at each pixel ground location, although the optical measurement geometry, described by the solar and viewing azimuth and zenith angles, varies strongly over the swath. However, the OMI retrieval algorithms are expected to determine the abundance of atmospheric trace gases irrespective of the optical measurement geometry irrespec-

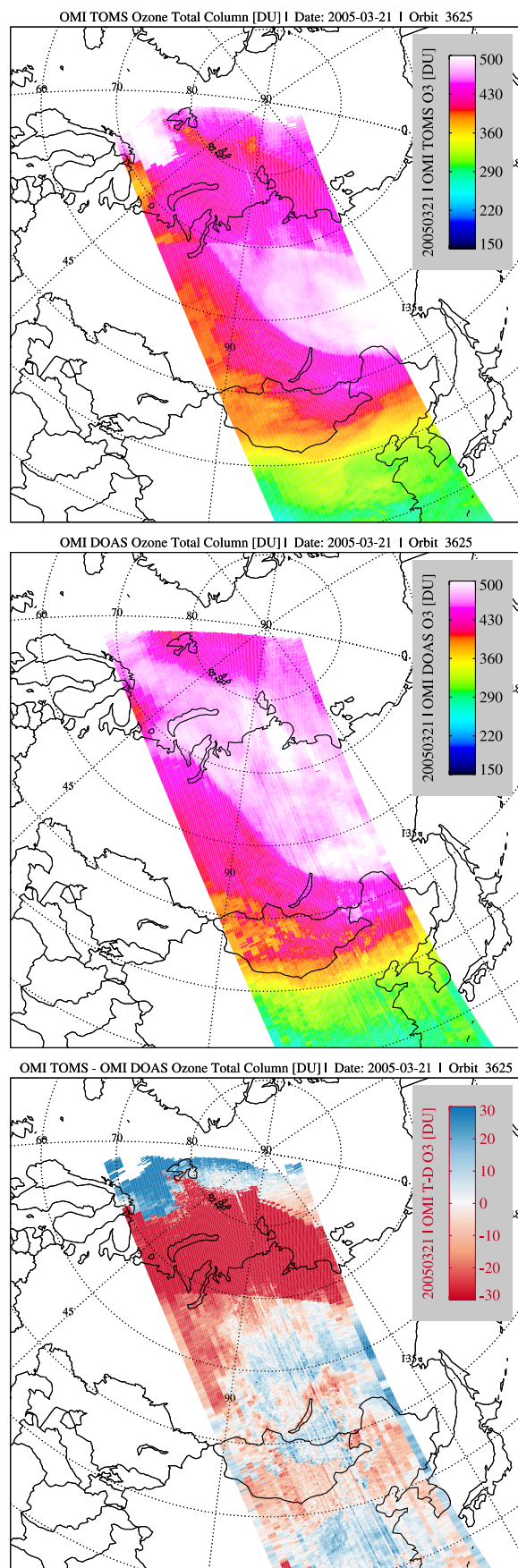


Figure 10. OMI-TOMS (top) and OMI-DOAS (middle) total ozone column and their difference (bottom) over the Northern Hemisphere for a single orbit 3625 recorded on 21 March 2005. Note the presence of a strong stepwise change ranging beyond -30 DU (or -10%) in OMI-TOMS that is absent in OMI-DOAS.

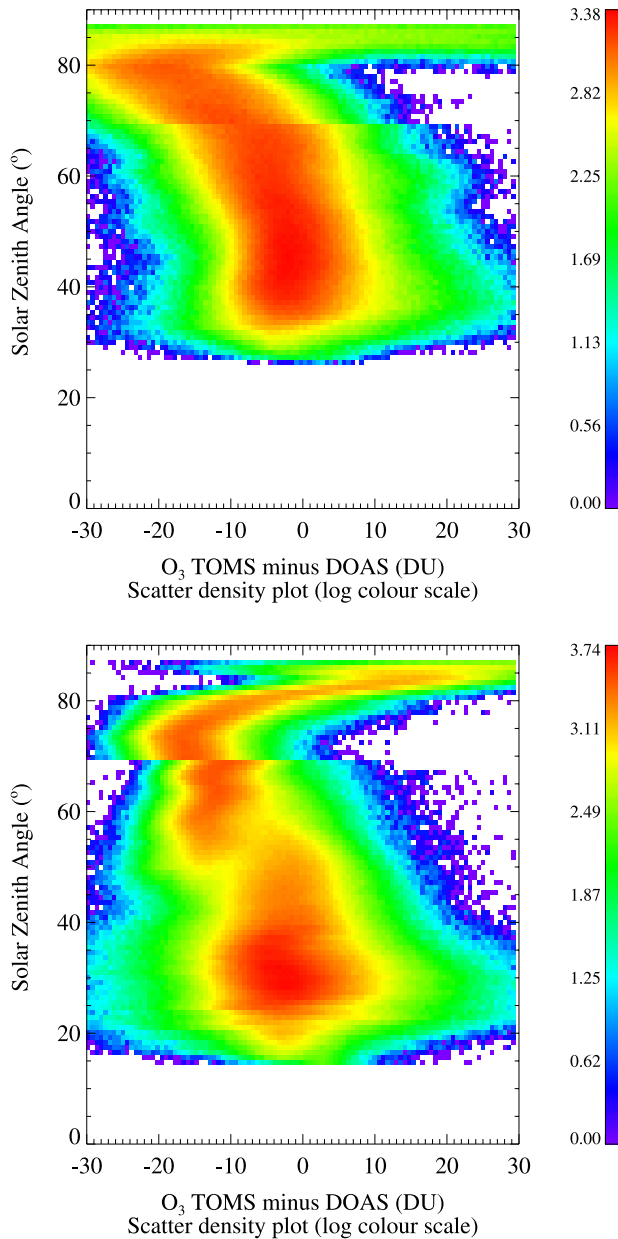


Figure 11. Logarithmic (base 10) scatter density plots of the solar zenith angle versus the total ozone column difference for the time period 14 to 20 December 2004 for the Northern (top) and Southern (bottom) hemispheres.

tive of the OMI cross track position. The CAMA toolbox generates along-track averages of all cross-track positions of the read data fields to check this assumption. Examples of global along-track averages for OMI-TOMS and OMI-DOAS total ozone columns are shown in Figure 7. From these graphs available for the OMI data record we conclude that the OMI total column ozone data products are independent of swath position.

4. Global Distributions of Total Ozone Column Difference

[11] Figure 8 shows the global distribution of the OMI total ozone column differences, in this paper calculated as

(OMI-TOMS minus OMI-DOAS). This image was generated using a week of data from the time period 14 to 27 October 2005, regrided to a latitude-longitude grid of $1.0^\circ \times 1.0^\circ$ resolution (180×360). Figure 8 reveals (1) the eruption of the Sierra Negra volcano in the east Pacific Ocean, Galapagos Islands, (2) a clear indication of the dependence on Antarctic sea ice, (3) significant differences in the northern high latitudes, and (4) a ring-shaped feature near 85°S , the diameter of which expands as the Sun rises over the South Pole. The features observed in the global total column ozone difference images vary significantly as a function of season, being influenced by surface albedo, snow and ice coverage, clouds, OMI observing angles, the position of the orbit terminators and episodic events such as volcanic eruptions.

[12] Figure 9 provides the total ozone column difference and its standard deviation for the OMI data record for the whole globe and for the Northern and Southern hemispheres separately. On the global scale, OMI-DOAS reports 0–8 DU more total ozone column than OMI-TOMS, depending on the season. Differences are largest during late spring (May) and early summer (June). The standard deviation of the total ozone column difference is considerably smaller than the standard deviation of the total ozone columns alone and also depends on the season. The Northern Hemisphere clearly dominates the global behavior of the total ozone column difference while the Southern Hemisphere shows tranquil behavior with time.

[13] Images constructed from regrided total column ozone difference data reveal the presence of various ring-shaped features at the high latitudes in the Northern and Southern hemispheres. To investigate the origin of these features, individual orbits have been analyzed. Figure 10 shows the OMI-TOMS and OMI-DOAS total ozone column in the Northern Hemisphere for a single orbit 3625 recorded on 21 March 2005. In this image OMI-TOMS shows a discontinuity which is absent in OMI-DOAS. Figure 10 also shows that the discontinuity can exceed 40 DU. This discontinuity occurs at 70° solar zenith angle where the TOMS V8 algorithm starts to use 313 nm measurements to correct for errors due to variations in ozone profile from climatology. Recent results indicate that a large part of this discontinuity is caused by stray light caused errors in the OMI measurements at 313 nm. It will be corrected when the OMI data are reprocessed using collection 3. However, smaller discontinuities are also present in the TOMS data; they could be due to relative errors in laboratory measured ozone cross sections or some other unknown cause. The ring-like feature closer to the terminator has been identified as error in the calculation of the air mass factor in the OMI-DOAS algorithm largely due to an erroneous correction for the spherical atmosphere.

5. Solar Zenith Angle

[14] In Figure 11 we present scatter density plots of the solar zenith angle versus the total ozone column difference. These graphs again reveal the presence of a discontinuity at 70° solar zenith angle. Beyond 70° solar zenith angle the differences vary strongly as a function of solar zenith angle with the strong swing to high values close to 87° being caused by the error in the OMI-DOAS air mass factor. In

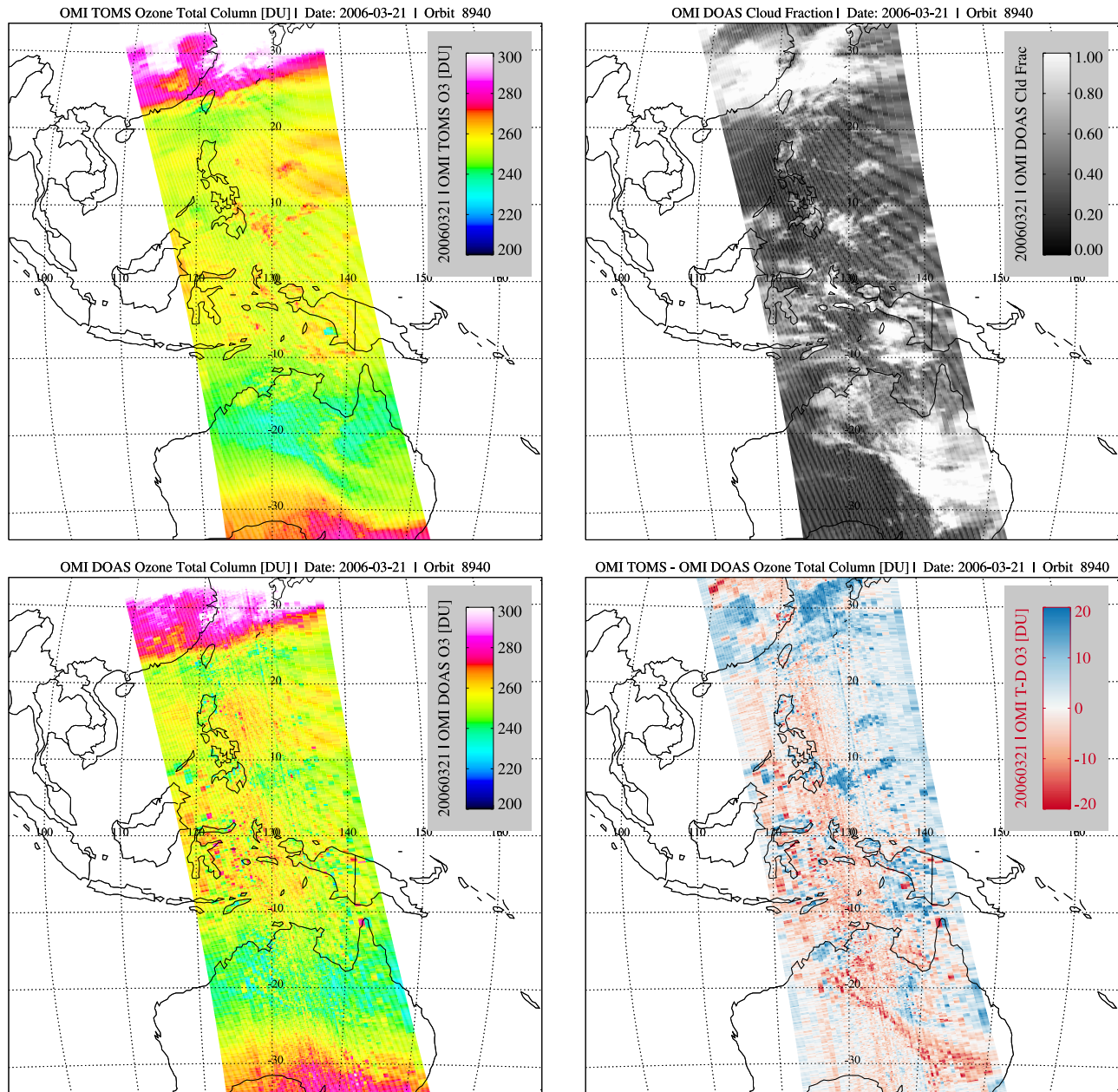


Figure 12. Single orbit plots for OMI orbit 8940 over tropical regions recorded on 21 March 2006 of the OMI-TOMS (top left) and OMI-DOAS (bottom left) total ozone columns, OMI-DOAS cloud fraction (top right) and OMI total ozone column difference (bottom right). Note the similarities of small-scale structures observed in the total ozone column difference with the cloud fraction and the OMI-TOMS total ozone field, where the dynamic range of the ozone field plots has been adjusted to enhance the observed cloud structures.

addition, there is also a steady trend in the total ozone column difference over the range 30° – 70° in solar zenith angle, being caused by the same shortcoming. In summary, this particular plot reveals several algorithm features that deserve improvements. At the time of writing new air mass factor tables have been calculated for OMI-DOAS on the basis of improved radiative transfer calculations. These improvements include a method to specifically deal with elastic (Cabannes) and inelastic (Cabannes) scattering.

These solutions will be incorporated in reprocessing the OMI-DOAS data record into collection 3.

6. Clouds

[15] Plotting total ozone columns for single OMI orbits over tropical regions reveals the presence of small-scale structures in OMI-TOMS data which appear to be absent in OMI-DOAS data. Figure 12 shows single orbit plots for OMI data products for orbit 8940 over tropical regions

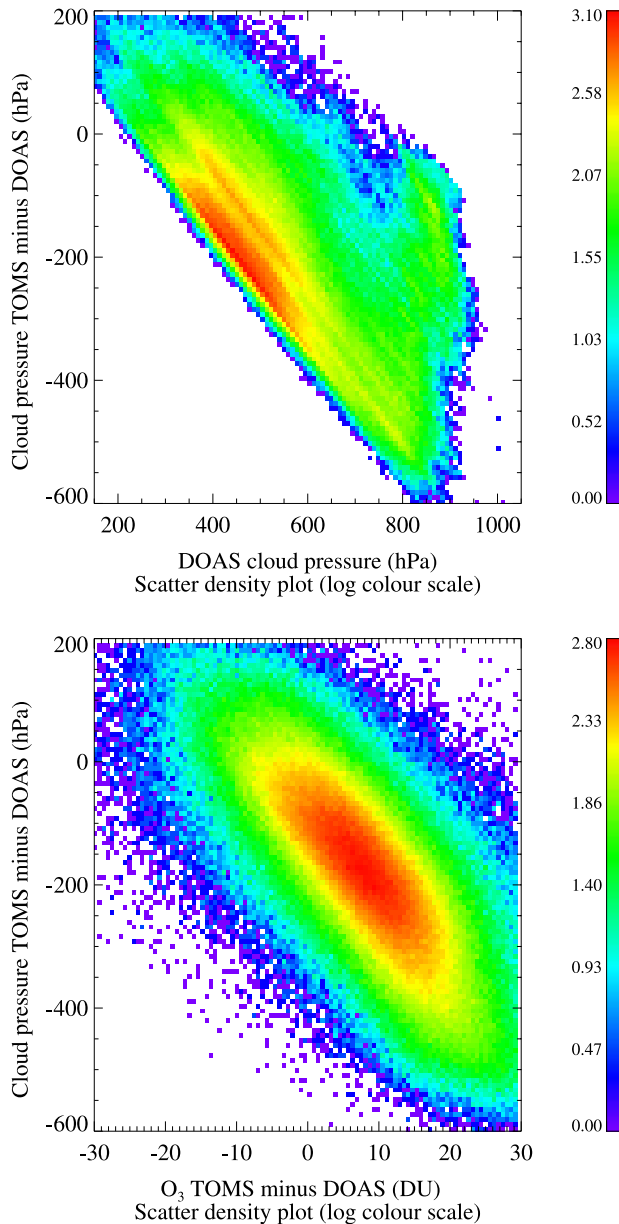


Figure 13. Logarithmic (base 10) scatter density plots of the OMI-TOMS and OMI-DOAS cloud pressure difference versus the OMI-DOAS cloud pressure (top) and versus the OMI-TOMS and OMI-DOAS total ozone column difference (bottom). Correlation coefficients are $R = -0.79$ and $R = -0.67$ for Figure 13 top and bottom, respectively.

recorded on 21 March 2006. The similarities of small-scale structures observed in the total ozone column difference with the cloud fraction and the OMI-TOMS total ozone field led to investigating the correlation of total ozone column data with cloud fraction and pressure. No significant correlations were found between total ozone column data and cloud fraction and cloud top pressure data. Furthermore, the OMI total ozone column difference showed no correlation with OMI-TOMS or OMI-DOAS cloud fraction or their cloud fraction difference. For cloud fractions lower than 5%, OMI-TOMS and OMI-DOAS total ozone columns are similar down to the 1.0 DU level. However, there is a

clear correlation with the difference in the cloud pressure assumed by the two algorithms, as shown in Figure 13.

[16] The OMI-TOMS algorithm uses a cloud top pressure climatology that was derived from a thermal infrared (TIR) sensor (THIR) that flew on the Nimbus-7 satellite in the 1980s. In deriving this climatology only bright clouds were used to avoid biasing the results by thin cirrus that have virtually no effect on UV but affect TIR significantly. This information is used by the TOMS algorithm to correct the OMI radiances for the Ring Effect, for the O_2-O_2 absorption at 360 nm, for enhanced ozone absorption above clouds due to multiple scattering, and for reduced absorption below clouds. By happenstance all these effects are of the same sign at wavelengths used in the TOMS V8 algorithm, making this algorithm more sensitive to error in cloud height than if some other wavelengths had been used in designing the TOMS instrument. In addition, the OMI-DOAS algorithm uses an effective cloud pressure estimated from the OMI data itself using the 470 nm O_2-O_2 absorption band. These cloud pressures are on the average 200–300 hPa larger than those reported by TIR sensors (Figure 13). This difference is caused by the fact that the outgoing radiation at the UV/Visible wavelengths is less sensitive to ice clouds than at TIR wavelengths, and thus OMI more often sees the lower-level water clouds. OMI-TOMS data processed using O_2-O_2 derived cloud pressures produce essentially the same results over clouds as does OMI-DOAS. Since we believe that OMI-derived effective cloud pressures are more appropriate for analyzing UV/Visible radiance data than those provided by TIR sensors, the next version of the TOMS algorithm will be based on cloud effective pressure climatology derived from OMI, rather than TIR-derived cloud top pressures.

7. Striping Features

[17] Zooming in on the dynamic range of ozone columns in the tropics actually enhances the appearance of the striping features as observed in the OMI-DOAS total ozone column plots of Figure 12. The largest contribution to these stripes is caused by insufficient dark current correction of the solar irradiance measurements. The dark current variations are picked up by the OMI CCD detectors when they are hit by cosmic radiation. In the ECS collection 2 data, on which this paper is based, the dark current was assumed to be constant over several weeks, however, this turned out not to be sufficient. For the collection 3, the dark current maps will be updated on a daily basis, which is expected to give much better results [Dobber *et al.*, 2008]. The reason that the OMI-DOAS total ozone shows more stripes than the OMI-TOMS data is because the DOAS implementation is using smaller variations in the ozone absorption which are more strongly affected by the dark current than are the OMI-TOMS bands. In addition, for OMI-TOMS correction techniques known as “soft calibration” are applied as a function of cross track position that very effectively reduce striping. Soft calibration is based on the principle that wavelength-dependent calibration can be inferred from the requirement that ozone derived at different wavelengths must be consistent. For OMI-DOAS in the ECS collection 2 starting with software version 1.0.1 from October 2005 onward, a fixed irradiance is used, which has been

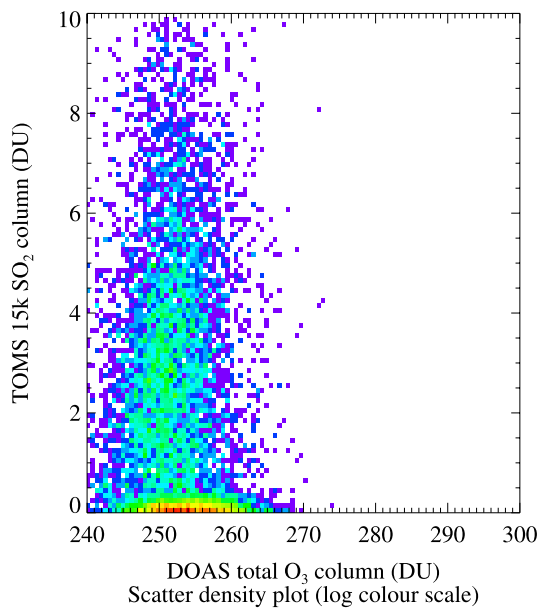
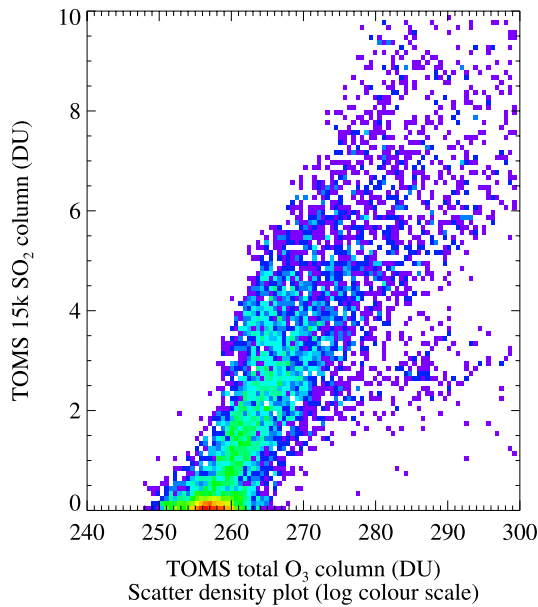


Figure 14. Logarithmic (base 10) scatter density plots of the OMI-SO₂ 15 km total sulfur dioxide column versus OMI-TOMS (top) and OMI-DOAS (bottom) total ozone columns for the region around the volcano Sierra Negra on Isla Isabelle. Note the strong dependence of OMI-TOMS on the total sulfur dioxide column and the absence of this dependence for OMI-DOAS.

derived from many irradiance measurements using a median filter. This approach also was a great improvement for reducing the striping features. The absolute differences in total ozone column values between these approaches are minor, much smaller than the retrieval accuracy, by which we consider the OMI-DOAS data record as continuous.

8. Volcanic Eruptions

[18] During the OMI data record time period several volcanoes erupted explosively such as Mount Etna in Italy,

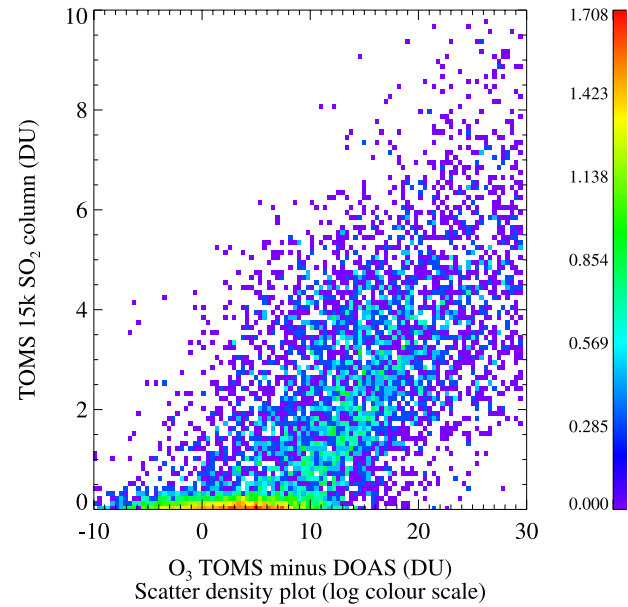


Figure 15. Logarithmic (base 10) scatter density plots of the OMI-SO₂ 15 km total sulfur dioxide column versus the difference of OMI-TOMS and OMI-DOAS total ozone columns for the region around the volcano Sierra Negra on Isla Isabelle. The structures and dependence of OMI-TOMS on the total sulfur dioxide column propagate into this graph.

Sierra Negra on the Galapagos Islands and Anatahan in the Mariana Archipelago. The exact moment of volcanic eruptions can be retrieved from the Earth Observatory Web site where OMI observations from the sulfur dioxide (SO₂) data product [Carn *et al.*, 2007] are regularly posted (August 2005: Anatahan, Mariana Islands, United States, available at http://earthobservatory.nasa.gov/NaturalHazards/natural_hazards_v2.php3?img_id=13043; October 2005: Sierra Negra, Galapagos Islands, Ecuador, available at http://earthobservatory.nasa.gov/NaturalHazards/natural_hazards_v2.php3?img_id=13253). The occurrence of large values in certain regions of global images of the OMI total ozone column difference seems to temporally and spatially coincide with these volcanic eruptions, an example of which is shown in Figure 8. A strongly positive and irregularly shaped feature appears in the east Pacific Ocean near the Galapagos Islands around the time of the main eruption. The reasoning above leads us to believe that volcanic eruptions are visible in the OMI total ozone column difference.

Table 1. Statistical Correlations of OMI Total Ozone Column and Total Sulfur Dioxide Column Data Products for the Selected Region Around the Sierra Negra Volcano for the Time Period 21 to 31 October 2005^a

	OMI-DOAS	OMI-TOMS	Delta-O ₃	OMI-SO ₂ , 15 km
OMI-DOAS	1.00	−0.0132	−0.395	−0.0540
OMI-TOMS	−0.0132	1.00	0.924	0.663
Delta-O ₃	−0.395	0.924	1.00	0.628
OMI-SO ₂ , 15 km	−0.0540	0.663	0.628	1.00

^aHere Delta-O₃ denotes total ozone column difference calculated as Ozone Monitoring Instrument–Total Ozone Mapping Spectrometer (OMI-TOMS)/OMI–Differential Optical Absorption Spectroscopy (DOAS). Note the similar high correlation of OMI-TOMS and Delta-O₃ with the OMI-SO₂ data products, where OMI-DOAS does not correlate well at all.

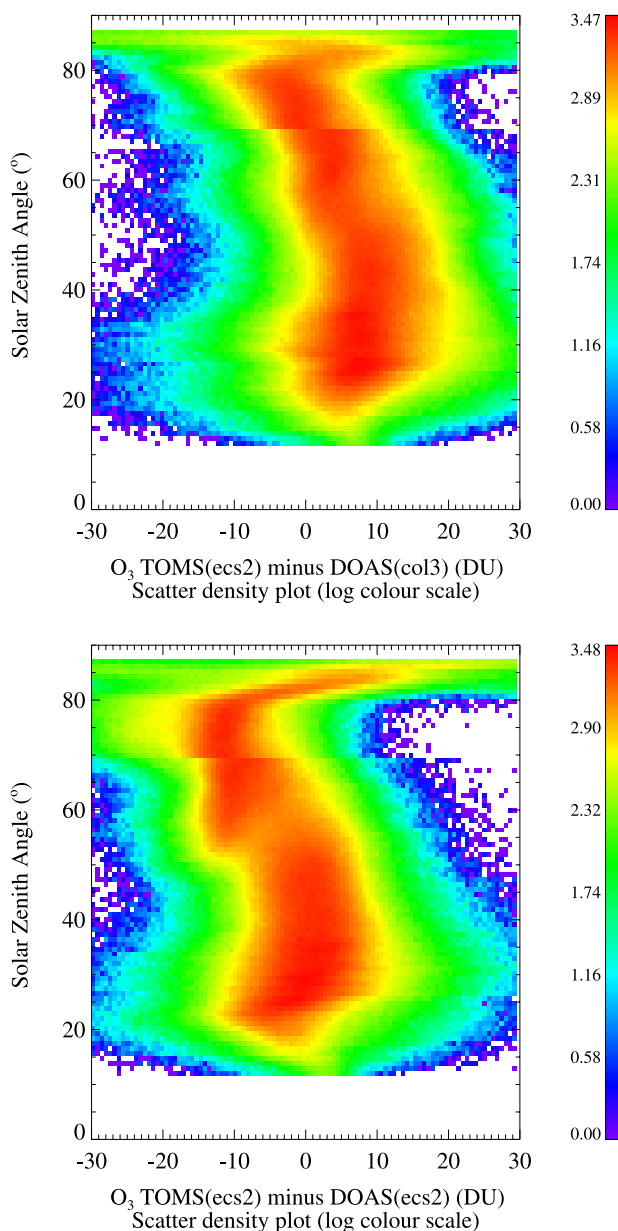


Figure 16. Logarithmic (base 10) scatter density plot of the solar zenith angle versus the total ozone column difference for the time period 13 to 15 January 2006 for the whole globe, incorporating the new (top) and operational (bottom) OMI-DOAS data product. Here DOAS(col3) denotes the latest OMI-DOAS algorithm version ready for collection 3 reprocessing. DOAS(ec2) and TOMS(ec2) denote the operational OMI-DOAS and OMI-TOMS data. Note the reduction of the dramatic swing above 70° SZA as observed in collection 2.

[19] Volcanic eruptions are often accompanied by emissions of large amounts of debris and volatiles. Volcanic debris consists of (1) lapilli, blocks and bombs, particles typically larger than 5 mm that are quickly deposited near the vent, and (2) ash particles (<1 mm) that may settle at considerable distances around the vent. The finest volcanic ash can remain airborne for long periods of time. Typical volcanic gases include water, carbon oxides, nitrogen

oxides, sulfur oxides, hydrogen chloride and halogen gases (fluorine, chlorine). Here we focus on examining the correlation between the observed features in the OMI total ozone column difference plots and the total sulfur dioxide column, an OMI data product [Carn *et al.*, 2007]. The correlation with aerosols will be established once the OMI aerosol data products are validated.

[20] Our case study involves the eruption of the Sierra Negra volcano on Isla Isabella, Galapagos, Ecuador, in the time period 21 to 31 October 2005. Calculations were limited to a region around the volcanic island covering the range 4.66°S to 3.00°N in latitude and 100.5°W to 87.8°W in longitude, to highlight this localized effect otherwise obscured in the global average. We computed statistical correlations between OMI-TOMS, OMI-DOAS, OMI total ozone column difference and OMI total sulfur dioxide columns. The OMI-SO₂ data product contains estimates of the total sulfur dioxide columns assuming three different altitude ranges where sulfur dioxide could reside in the atmosphere. In view of the explosive nature of the Sierra Negra volcano, the OMI-SO₂ 15 km data are considered in this case study. OMI-TOMS total ozone column data were filtered for the flag “quality flags” that denotes possible contamination with sulfur dioxide when set to a value of “5”, the binary code 101 of the lowest three bits.

[21] Figure 14 shows the scatter density plot of the OMI-SO₂ 15 km total sulfur dioxide column versus OMI-TOMS and OMI-DOAS total ozone columns for the region and time period of interest. The OMI-TOMS total column ozone plot reveals a strong dependence of total column ozone on the total sulfur dioxide column where OMI-DOAS does not. OMI-TOMS total ozone column is found to correlate well with the sulfur dioxide column as does the OMI total ozone difference, as seen from Figure 15, where OMI-DOAS does not. Finally, the values of the correlation coefficients presented in Table 1 support these observations. Values beyond 0.65 for OMI-TOMS and close to zero for OMI-DOAS lead to conclude that the effect can be attributed to OMI-TOMS. Most probably the OMI-TOMS total ozone column retrieval algorithm does not adequately distinguish between strong absorption features of ozone or sulfur dioxide because of the use of selective wavelength bands where these features coincide. This is a known fact for older ground based Dobson instruments as well [De Muer and De Backer, 1994]. Enhanced concentrations of sulfur dioxide are represented as enhanced concentrations of ozone because the absorption features of both molecules fall in the wavelength range over which the instruments perform an integration of the measured intensities. The OMI-DOAS retrieval algorithm on the other hand uses the OMI spectral resolution to its fullest to distinguish between the spectral signatures of ozone and sulfur dioxide. In fact, the region where OMI derives ozone is at a minimum in the sulfur dioxide spectrum and in that region there is comparatively little structure.

9. Outlook to OMI Collection 3 Total Ozone Column Data

[22] On the basis of a comprehensive effort for improving the quality and understanding of the OMI instrument calibration by performing in-flight calibration investiga-

tions, the OMI calibration team has delivered a data set of optimal parameter choices of the entire OMI data record [Dobber *et al.*, 2008]. With this data set all OMI Level-0 data will be reprocessed toward a new collection of OMI level 1B data and subsequent to OMI level 2 data that will be labeled collection 3. Major improvements of this level 1B collection are (1) sophisticated and optimized radiometric calibration, (2) improved dark current corrections, and (3) improved stray light corrections. In addition, the level 2 retrieval algorithms will be optimized on the basis of validation results obtained with collection 2. For the OMI-DOAS total ozone column retrieval the most important changes are (1) a new air mass factor table to incorporate the spherical shape of the atmosphere and (2) a new scheme to deal with snow and ice covered surfaces. As part of testing these new developments, OMI-DOAS total ozone column collection 3 data were calculated for various time periods along the OMI data record. In Figure 16 we present preliminary results of comparing OMI-DOAS collections 3 against OMI-TOMS of collection 2 used as the baseline. The solar zenith angle dependence in the range of 30°–70° solar zenith angle has been significantly suppressed. More importantly, the improved air mass factor calculations for OMI-DOAS has removed the dramatic swing around 85°. Results obtained with polar-AVE data and OMI-DOAS collection 3 data have also shown that over bright snow covered surfaces at very high solar zenith angle, OMI-DOAS is performing as well as OMI-TOMS [Kroon *et al.*, 2008]. Please note that OMI-DOAS data of collection 2 and collection 3 are based on different OMI level 1B data sets.

10. Conclusions

[23] In this paper we present the results of a study on the similarities and differences between the output of the OMI-TOMS and OMI-DOAS total ozone retrieval algorithms that performed operational processing of collection 2 OMI data. The algorithms differ in many aspects which propagate in the behavior of the retrieved data products. This study has revealed the following:

[24] OMI-TOMS and OMI-DOAS total ozone values compare very well over the entire OMI data record. Global images reveal similar structures. Averaged over the globe, the OMI-TOMS retrievals differ by 0–9 DU (0–3%) with the OMI-DOAS retrieval, depending on season. Averaged over the OMI data record this global difference amounts to 3.7 DU. The good comparison of OMI-TOMS to OMI-DOAS total ozone values is further expressed by high-correlation coefficients, which hardly fall below 0.90 and often reach values close to unity. Regression analysis yields slopes that hardly fall below 0.90. Along-track averages of the OMI cross track positions reveal no significant structures in the OMI swath for either data product.

[25] In the tropics the OMI-TOMS and OMI-DOAS total ozone retrieval algorithms differ in the treatment of clouds. The OMI-TOMS algorithm relies on a TIR-derived cloud top pressure climatology which differs considerably from the OMI-derived effective cloud pressures that are used by OMI-DOAS. The differences appear to be due to the

difference in sensitivity of the two cloud algorithms to ice clouds.

[26] The OMI-TOMS total ozone retrieval algorithm shows a discontinuity at 70° solar zenith angle. This appears to be largely, though not entirely, due to OMI stray light effects that will be corrected in collection 3 reprocessing. Near the terminator the OMI-DOAS algorithm underestimates the total ozone column by more than 30 DU as compared to the OMI-TOMS total ozone retrieval algorithm. This behavior is now understood and will also be corrected during reprocessing. Preliminary results indicate that the reprocessing will bring the two algorithms in much better agreement.

[27] The OMI-TOMS retrieval algorithm, based on the TOMS V8 algorithm, appears to be a robust algorithm. Most of the cloud related errors appear correctable using a cloud climatology developed using OMI data. Differences between climatology and actual cloud pressures will produce a 1–2% random noise in OMI-TOMS data. Analysis shows that the 70° discontinuity problem can be minimized by selecting the algorithm switching point on the basis of slant ozone column rather than on solar zenith angle. The next version of the OMI-DOAS retrieval algorithm used in collection 3 reprocessing appears to be doing at least as well as OMI-TOMS under most conditions and is clearly better under certain conditions, e.g., in presence of volcanic SO₂. Similar analysis of reprocessed data from both algorithms will be conducted to identify any remaining weaknesses in the two algorithms. Comparison of total ozone data produced by OMI-TOMS and OMI-DOAS algorithms, as presented in this paper, has been very helpful in improving both algorithms. Some of the lessons learned on the basis of this paper can be applied retrospectively to improve the TOMS algorithm which will result in an improved long-term record of ozone from the TOMS instrument series starting in November 1978.

[28] **Acknowledgments.** The Dutch-Finnish built OMI instrument is part of the NASA EOS Aura satellite payload. The OMI project is managed by NIVR and KNMI in the Netherlands. OMI total ozone column data were processed at NASA and were obtained from the NASA Goddard Earth Sciences (GES) Data and Information Services Center (DISC). Send request for OMIE-KNMI documents to mark.kroon@knmi.nl or visit the OMI pages at <http://www.knmi.nl/omi>.

References

- Balis, D., M. Kroon, M. E. Koukouli, E. J. Brinksma, G. Labow, J. P. Veefkind, and R. D. McPeters (2007), Validation of Ozone Monitoring Instrument total ozone column measurements using Brewer and Dobson spectrophotometer ground-based observations, *J. Geophys. Res.*, **112**, D24S46, doi:10.1029/2007JD008796.
- Bhartia, P. K., and C. Wellemeyer (2002), TOMS-V8 total O₃ algorithm, in *OMI Algorithm Theoretical Basis Document*, vol. II, *OMI Ozone Products*, ATBD-OMI-02, edited by P. K. Bhartia, pp. 15–31, NASA Goddard Space Flight Cent., Greenbelt, Md. (Available at http://eospsoc.gsfc.nasa.gov/eos_homepage/for_scientists/atbd/index.php)
- Cam, S. A., N. A. Krotkov, K. Yang, R. M. Hoff, A. J. Prata, A. J. Krueger, S. C. Loughlin, and P. F. Levelt (2007), Extended observations of volcanic SO₂ and sulfate aerosol in the stratosphere, *Atmos. Chem. Phys. Discuss.*, **7**, 2857–2871.
- DeMuer, D., and H. DeBacker (1994), Influence of sulfur dioxide trends on Dobson measurements and on electrochemical ozone soundings, *Proc. SPIE Int. Soc. Opt. Eng.*, **2047**, 18–26.
- Dobber, M., Q. Kleipool, R. Dirksen, P. F. Levelt, G. Jaross, S. Taylor, T. Kelly, L. Flynn, G. Leppelmeier, and N. Rozemeijer (2008), Validation of Ozone Monitoring Instrument level 1b data products, *J. Geophys. Res.*, **113**, D15S06, doi:10.1029/2007JD008665.

- Kroon, M., I. Petropavlovskikh, R. Shetter, S. Hall, K. Ullmann, J. P. Veefkind, R. D. McPeters, E. V. Browell, and P. F. Levelt (2008), OMI total ozone column validation with Aura-AVE CAFS observations, *J. Geophys. Res.*, *113*, D15S13, doi:10.1029/2007JD008795.
- Levelt, P. F. (Ed.) (2002), *OMI Algorithm Theoretical Basis Document*, vol. I, *OMI Instrument, Level 0-1b Processor, Calibration and Operations, ATBD-OMI-01*, NASA Goddard Space Flight Cent., Greenbelt, Md. (Available at http://eosps.gsfc.nasa.gov/eos_homepage/for_scientists/atbd/docs/OMI/ATBD-OMI-01.pdf)
- Levelt, P. F., G. H. J. van den Oord, M. R. Dobber, A. Malkki, H. Visser, J. de Vries, P. Stammes, J. O. V. Lundell, and H. Saari (2006a), The Ozone Monitoring Instrument, *IEEE Trans. Geosci. Remote Sens.*, *44*(5), 1093–1101, doi:10.1109/TGRS.2006.872333.
- Levelt, P. F., E. Hilsenrath, G. W. Leppelmeier, G. H. J. van den Oord, P. K. Bhartia, J. Tamminen, J. F. de Haan, and J. P. Veefkind (2006b), Science objectives of the Ozone Monitoring Instrument, *IEEE Trans. Geosci. Remote Sens.*, *44*(5), 1199–1208, doi:10.1109/TGRS.2006.872336.
- McPeters, R., M. Kroon, G. Labow, E. Brinksma, D. Balis, I. Petropavlovskikh, J. P. Veefkind, P. K. Bhartia, and P. F. Levelt (2008), Validation of the Aura ozone monitoring instrument total column ozone product, *J. Geophys. Res.*, *113*, D15S14, doi:10.1029/2007JD008802.
- Perner, D., and U. Platt (1979), Detection of nitrous acid in the atmosphere by differential optical absorption, *Geophys. Res. Lett.*, *6*, 917–920, doi:10.1029/GL006i012p00917.
- Schoeberl, M. R., et al. (2006), Overview of the EOS aura mission, *IEEE Trans. Geosci. Remote Sens.*, *44*(5), 1066–1074, doi:10.1109/TGRS.2005.861950.
- Veefkind, J. P., J. F. de Haan, E. J. Brinksma, M. Kroon, and P. F. Levelt (2006), Total ozone from the Ozone Monitoring Instrument (OMI) using the OMI-DOAS technique, *IEEE Trans. Geosci. Remote Sens.*, *44*(5), 1239–1244.

P. K. Bhartia and R. D. McPeters, NASA Goddard Space Flight Center, Code 916, Greenbelt, MD 20771, USA.

M. Kroon, P. F. Levelt, M. Sneep, and J. P. Veefkind, Royal Netherlands Meteorological Institute, P. O. Box 201, NL-3730 AE De Bilt, Netherlands. (mark.kroon@knmi.nl)